PHYSICAL REVIEW A **100**, 033819 (2019)

Bandwidth and conversion efficiency analysis of dissipative Kerr soliton frequency combs based on bifurcation theory

J. Gärtner,[1] P. Trocha,[2] R. Mandel,[1] C. Koos,[2] T. Jahnke,[3] and W. Reichel[1,*]
[1]*Institute for Analysis (IANA), Karlsruhe Institute of Technology, 76131 Karlsruhe, Germany*
[2]*Institute of Photonics and Quantum Electronics (IPQ), Karlsruhe Institute of Technology, 76131 Karlsruhe, Germany*
[3]*Institute for Applied and Numerical Mathematics (IANM), Karlsruhe Institute of Technology, 76131 Karlsruhe, Germany*

(Received 21 December 2018; revised manuscript received 25 July 2019; published 13 September 2019)

Dissipative Kerr soliton frequency combs generated in high-Q microresonators may unlock novel perspectives in a variety of applications and crucially rely on quantitative models for systematic device design. Here, we present a global bifurcation study of the Lugiato-Lefever equation which describes Kerr comb formation. Our study allows systematic investigation of stationary comb states over a wide range of technically relevant parameters. Quantifying key performance parameters of bright and dark-soliton combs, our findings may serve as a design guideline for Kerr comb generators.

DOI: 10.1103/PhysRevA.100.033819

I. INTRODUCTION AND MAIN RESULTS

Kerr frequency combs have the potential to revolutionize a variety of applications such as high-speed data transmission [1–3], high-precision optical ranging [4,5] and spectroscopy, [6] as well as highly accurate optical frequency synthesis [7]. Kerr frequency combs stand out due to their high optical bandwidth that may exceed an octave of frequencies, narrow linewidths down to 1 kHz, and large line spacings of tens of GHz [8–10]. Moreover, Kerr comb generators feature a small footprint and are amenable to efficient wafer-level mass production, thereby paving the path to large-scale industrial deployment. On a physical level, Kerr comb generators rely on third-order nonlinear interaction in high-Q microresonators that are pumped by a continuous-wave (CW) laser [11]. Under appropriate pump conditions, cascaded degenerate and non-degenerate four-wave mixing can lead to a soliton waveform that circulates in the cavity, balancing self-phase modulation and dispersion, as well as cavity loss and parametric gain [12]. These dissipative Kerr soliton combs consist of strictly equidistant phase-locked optical tones and stand out due to smooth spectral envelopes and extraordinary robustness with respect to variations of the pump conditions.

Mathematically, Kerr frequency comb generators are represented by nonlinear systems with rather complex dynamics. Systematic design and theory-guided improvement of Kerr comb sources therefore require reliable mathematical models that cover practically relevant parameter spaces and that combine intuitive qualitative understanding with quantitatively correct predictions of the behavior of the nonlinear system. Kerr comb dynamics are described by the Lugiato-Lefever equation (LLE), a damped, driven and detuned nonlinear Schrödinger equation [13–15]. The LLE has been extensively studied, using, e.g., numerical simulations of the temporal comb formation dynamics, which have reached remarkable accuracy in predicting and explaining experimental results [16,17]. However, time-domain integration of the LLE only allows to access specific comb states that strongly depend on the individual device parameters as well as on the complex interplay of the initial conditions and the time-dependent tuning of the pump. Specifically, time-integration techniques do not permit us to globally study the variety of different stationary Kerr comb states that can be accessed by exploiting the full range of technically accessible device and operation parameters. This gap can be closed by bifurcation analysis, which allows us to investigate the structure of stationary solutions and to obtain qualitative as well as quantitative insights. So far, stationary states of the LLE have been mainly investigated by local bifurcation analysis [14,15,18–24], focusing on states in the vicinity of the trivial LLE solution that consists of a single CW tone at the pumped resonance. Global aspects, in particular, concerning the snaking behavior of solution branches are discussed in Refs. [15,19,20] and, recently, a rigorous stability analysis of stationary states closing the gap between linearized stability and nonlinear stability was achieved in Ref. [25]. These methods revealed a large variety of comb states, and were partially extended via numerical continuation methods to regions further away from the trivial state where solitons occur. However, a global study that identifies pronounced soliton states and favorable operation regimes across the full range of technical accessible device and operation parameters has not been presented so far.

In this paper, we present a global bifurcation study of the LLE, covering a large space of technically accessible parameters. Our analysis comprises both bright-soliton (BS) states in resonators with anomalous group-velocity dispersion (GVD) [12] as well as dark-soliton (DS) states that form in the presence of normal GVD [26]. For both types of combs, we classify branches associated with single and multisoliton states and characterize single-soliton states by their optical bandwidth as well as by the pump-to-comb power transfer efficiency. Our bifurcation analysis hence allows determining and systematically optimizing the performance of Kerr comb

---

[*] wolfgang.reichel@kit.edu

generators in integrated photonic systems, which is of significant importance for industrial adoption of these devices.

This paper is organized as follows: In Sec. II, we introduce the LLE and derive sufficient conditions for bifurcations from the trivial state. In Sec. III, we identify bifurcation branches leading to single-soliton states and investigate the behavior of the soliton and its characteristics along these branches. Section IV is dedicated to a quantitative characterization of single-soliton frequency combs using the bandwidth and the power conversion efficiency as performance metrics. Mathematical details and derivations can be found in Appendices A–E.

II. BIFURCATION ANALYSIS FOR THE LUGIATO-LEFEVER EQUATION

We start our our analysis from the LLE,

$$\mathrm{i}\frac{\partial a}{\partial t} = -da'' - (\mathrm{i} - \zeta)a - |a|^2 a + \mathrm{i}f, \tag{1}$$

and its stationary version,

$$-da'' - (\mathrm{i} - \zeta)a - |a|^2 a + \mathrm{i}f = 0. \tag{2}$$

Here, $a(t, x)$ represents the optical intracavity field as a function of normalized time t and angular position $x \in [0, 2\pi]$ within the cavity. Hence a is 2π-periodic with respect to x. Moreover, d is the GVD parameter, and ζ the detuning of the input pump laser as a free real-valued parameter. The forcing f corresponds to the amplitude of the optical driving field. Relations that connect the normalized quantities d, ζ, f to their physical counterparts can be found in Appendix D. In the following, we consider 2π-periodic solutions a of Eq. (2), which feature even symmetry about $x = \pi$ and therefore fulfill the Neumann boundary conditions:

$$a'(0) = a'(\pi) = 0. \tag{3}$$

Thus, from now on we restrict our attention to functions $a : [0, 2\pi] \to \mathbb{C}$, which satisfy Eq. (2) on $[0, \pi]$ together with Eq. (3) and are evenly reflected around $x = \pi$. In Fourier modes, the solution is represented as $a(x) = \sum_{k\in\mathbb{Z}} \hat{a}_k \mathrm{e}^{\mathrm{i}kx}$ with $\hat{a}_{-k} = \hat{a}_k$. The intracavity power of the field is given by the square of the L^2-norm $\|a\|_2^2 := \sum_{k\in\mathbb{Z}} |\hat{a}_k|^2$. There are trivial solutions a_0 of Eqs. (2) and (3) which are complex constants. Let us assume that the trivial solution a_0 can be parametrized (locally) as $a_0 = a_0(\zeta)$[1]. As an example, the curve $(\zeta, a_0(\zeta))$ of constant solutions is shown in black for $f = 2$ in Fig. 1(a) in the case of anomalous dispersion ($d = 0.1$) and in Fig. 1(d) in the case of normal dispersion ($d = -0.1$). For each ζ, the squared L^2-norm of $a_0(\zeta)$ is plotted.[2] Note that three different constant solutions exist for certain values of ζ. Nontrivial solutions associated with frequency combs may arise from the curve of trivial solutions at bifurcation points, which can be defined in the simplest form applicable for our purposes as follows: *A point $P = (\zeta_0, a_0(\zeta_0)) \in \mathbb{R} \times \mathbb{C}$ on the trivial curve is called a bifurcation point for Eqs. (2) and (3) if there exists a second curve (ζ_s, a_s) of solutions of Eqs. (2) and (3), which is parameterized by s in some interval and crosses transversally the trivial curve at P.*

The structure of the solution set near $(\zeta_0, a_0(\zeta_0))$ depends on the properties of the *linearized operator L*, defined by

$$L\phi := -d\phi'' - (\mathrm{i} - \zeta_0)\phi - 2|a_0|^2\phi - a_0^2\bar{\phi}, \tag{4a}$$

$$\phi'(0) = \phi'(\pi) = 0, \tag{4b}$$

where we write a_0 instead of $a_0(\zeta_0)$. The spectrum of L consists of countably many complex eigenvalues whose real parts tend to $+\infty$ in the case $d > 0$ and to $-\infty$ in the case $d < 0$. This can be shown via Fourier series expansion as in Ref. [21, Proposition 4.3]. Because of the implicit function theorem, cf. Ref. [27, Theorem I.1.1], nontrivial solutions can only bifurcate from the trivial branch at $(\zeta_0, a_0(\zeta_0))$ if the kernel $\operatorname{Ker} L = \{\phi : L\phi = 0, \phi'(0) = \phi'(\pi) = 0\}$ is at least one-dimensional. This is the case provided that there is an integer $k \in \mathbb{N}$ such that

$$(\zeta_0 + dk^2)^2 - 4|a_0(\zeta_0)|^2(\zeta_0 + dk^2) + 1 + 3|a_0(\zeta_0)|^4 = 0. \tag{5}$$

Solving Eq. (5) yields

$$k_{1,2} := \sqrt{\frac{2|a_0(\zeta_0)|^2 - \zeta_0 \pm \sqrt{|a_0(\zeta_0)|^4 - 1}}{d}}. \tag{6}$$

For details on the derivation of Eqs. (5) and (6), see Appendix A. The wave number $k_{1,2}$ obtained by evaluating the expression on the right side of Eq. (6) defines the angular periodicity $2\pi/k_{1,2}$, after which the nontrivial comb state in the vicinity of the bifurcation point repeats itself, i.e., $a(x) = a(x + 2\pi/k_{1,2})$. Equations (5) and (6) naturally occur in bifurcation studies of Eq. (2). In Refs. [14,15,19,24], for instance, bifurcations are considered from the point of view of spatial dynamics both for normal and anomalous dispersion, and parameter regimes are determined where Turing patterns as well as 1-soliton states bifurcate from trivial solutions. In Ref. [20], a similar approach is taken to study bifurcation of DSs from trivial solutions in the normal-dispersion regime. In most of these works, local bifurcations from the trivial solution family are determined analytically and a numerical global bifurcation analysis is performed for periodic solutions (cf. Refs. [15,19,20,24]). Typically, the forcing parameter f is taken as the bifurcation parameter. In contrast, we study global bifurcations of 2π-periodic solutions with respect to the detuning ζ, whose physically accessible parameter space is usually larger than the parameter space for f. Our central goal is the localization of the most pronounced 1-solitons in the global bifurcation picture. With the help of Eq. (6), we can formulate the following bifurcation result, which explains under what conditions bifurcations from the line of trivial solutions occur:

For a point $P = (\zeta_0, a_0(\zeta_0))$ on the curve of trivial solutions, the following is true:

---

[1] This assumption is for simplicity of the presentation. It fails only at the turning points of the trivial curve, which does not lead to any undesirable effect. Other parametrizations $\zeta_0 = \zeta_0(t) = f^2(1 - t^2) + \frac{t}{\sqrt{1-t^2}}$, $a_0 = a_0(t) = f(1 - t^2) - \mathrm{i}ft\sqrt{1 - t^2}$ with $t \in (-1, 1)$ are also possible, cf. Ref. [21].

[2] In all figures, units on axes are dimensionless.

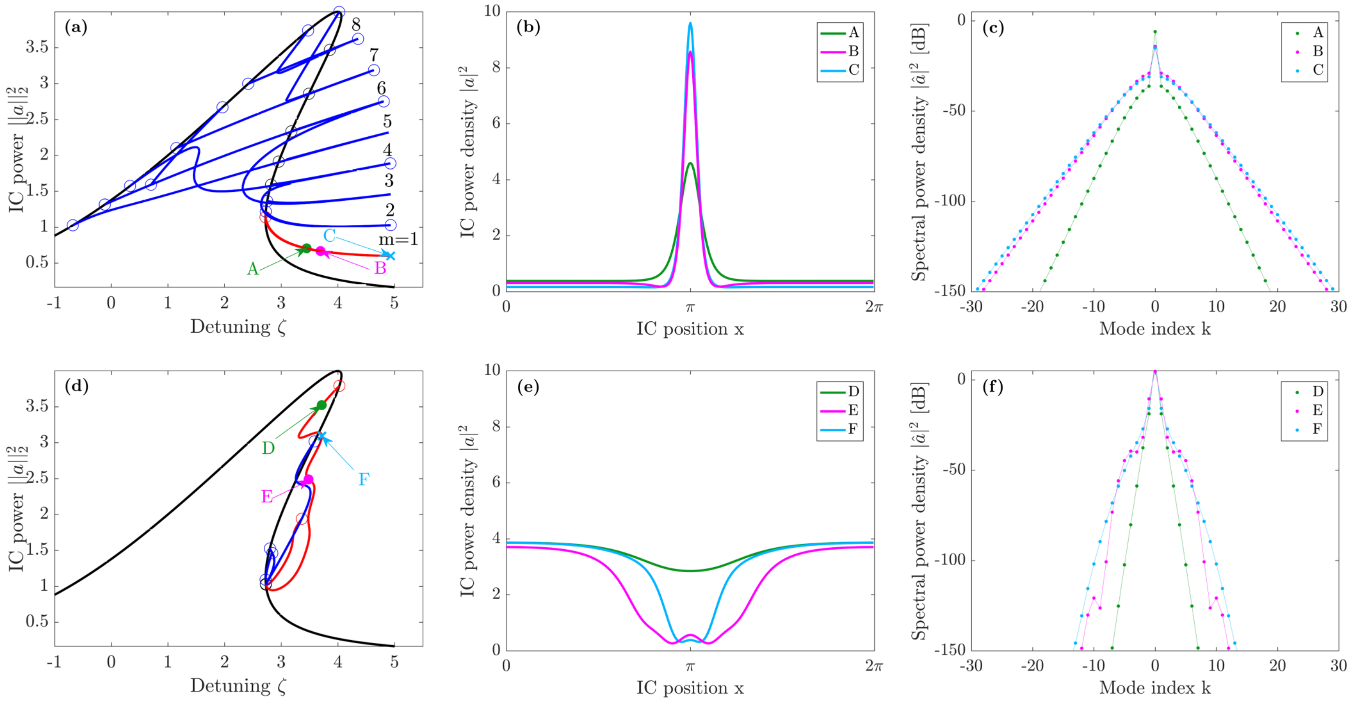

FIG. 1. Bifurcation maps and nontrivial comb states for bright solitons in anomalous-dispersion ($d > 0$, top) and dark solitons in normal-dispersion microresonators ($d < 0$, bottom). Quantities on axes are dimensionless. (a) Bifurcation map of the LLE for $f = 2$ and $d = 0.1$, indicating the normalized intracavity power $||a||_2^2$ vs. the normalized detuning ζ. The constant solution is indicated in black, the single soliton state bifurcation branch ($m = 1$) in red, while blue corresponds to other bifurcation branches of multisoliton states with $m = 2, \dots, 8$ pulses circulating in the cavity. Circles indicate bifurcation points. (b) Spatial power distribution as a function of normalized intracavity position x of single-soliton states corresponding to points A, B, and to the turning point C indicated in (a). (c) Spectral power distribution of single-soliton states corresponding to points A, B, and to the turning point C indicated in (a). Note that for illustrative purposes, a relatively low forcing $f = 2$ was chosen, resulting in a quick drop of the power of spectral modes further away from the pump. Here the bifurcation-and-continuation method is sufficiently precise to correctly predict spectral components which are more than 150 dB below the pump, hence safely covering technical relevant power ranges. (d) Bifurcation map of the LLE for $f = 2$ and $d = -0.1$, indicating the normalized intracavity power $||a||_2^2$ vs the normalized detuning ζ. Black denotes again the constant solution, red the single-soliton state bifurcation branch, and blue corresponds to other bifurcation branches. Here, circles also mark bifurcation points. (e) Spatial power distribution as a function of normalized intracavity position x of single-soliton states corresponding to points D, E, and to the turning point F indicated in (d). (f) Spectral power distribution of single-soliton states corresponding to points D, E, and to the turning point F indicated in (d).

(i) *If exactly one of the two numbers* $k_{1,2}$ *from Eq. (6) is an integer and if the transversality condition*

$$2|a_0(\zeta_0)|^4(|a_0(\zeta_0)|^2-\zeta_0) \mp(1+\zeta_0^2-|a_0(\zeta_0)|^4)\sqrt{|a_0(\zeta_0)|^4-1}\neq 0 \qquad (7)$$

holds with $-$ *if* $k_1 \in \mathbb{N}$ *and* $+$ *if* $k_2 \in \mathbb{N}$, *then* P *is a bifurcation point for Eqs. (2) and (3).*

(ii) *If neither* k_1 *nor* k_2 *is an integer, then* P *is not a bifurcation point for Eqs. (2) and (3), and near* P *only trivial solutions of Eqs. (2) and (3) exist.*

In the remaining cases, where either the condition from Eq. (7) fails or both k_1 and k_2 are integers, no statement can be made. Let us add that Eq. (7) is in general not implied by Eq. (6) and therefore has to be checked separately. The above result mainly goes back to Theorem 4 in [21]. Compared to Ref. [21], its present formulation as well as its proof allow substantial simplifications as we will show in Appendix B. Computations reveal that our bifurcation points on the trivial solution family are either of center or of saddle center type in the language of spatial dynamics as used, e.g., in Ref. [20, Table 1]. To see this, notice that for the bifurcation of periodic solutions from a constant solution y_0 of $y' = F(y)$, $y = (\mathrm{Re}\, a, \mathrm{Im}\, a, \mathrm{Re}\, a', \mathrm{Im}\, a')$ at least one pair of purely imaginary eigenvalues of $F'(y_0)$ is necessary. The eigenvalues λ of $F'(y_0)$ solve Eq. (5) with k replaced by $\pm i\lambda$, and the solutions $e^{\lambda x}(v_1, v_2, v_3, v_4)$ of the linearized spatial dynamics system correspond to solutions $\cos(kx)(v_1 + iv_2)$ in the kernel of L as defined in Eqs. (4).

For the cases $f = 2$ and $d = \pm 0.1$, we numerically computed the bifurcation points determined by Eq. (5). We also checked, for all bifurcation points, which of the numbers $k_{1,2}$ in Eq. (6) is an integer, and whether the transversality condition from Eq. (7) holds, cf. Table I. The computed bifurcation points on the trivial branch are marked by circles in Figs. 1(a) and 1(d) for $d = 0.1$ and $d = -0.1$, respectively. In case (i) of the above result, we may apply Rabinowitz's global bifurcation theorem from Ref. [28]. As a result, we obtain that a branch bifurcating from the trivial curve at $(\zeta_0, a_0(\zeta_0))$ either returns to the trivial curve at some other bifurcation point or joins another branch of nontrivial solutions, since unbounded branches are excluded due to Theorems 1 and 2 in Ref. [21].

In Fig. 1(a), a complete picture of all branches bifurcating from the trivial branch is shown for anomalous dispersion

TABLE I. Bifurcation points on the trivial branch for anomalous dispersion $d = 0.1$, $f = 2$. The coordinates $(\zeta_0, a_0(\zeta_0))$ shown in the first two columns are determined so at least one of the values $k_{1,2}$ (third and fourth columns) from Eq. (6) is an integer. The integer value of either k_1 or k_2 determines the periodicity of the field in the vicinity of the corresponding bifurcation point. The last column lists the values obtained from evaluating the left side of Eq. (7) to determine whether the transversality condition is fulfilled.

ζ_0	$a_0(\zeta_0)$	k_1	k_2	Transv.
−0.6770	0.51 + 0.87i	5.44	5	3.67
−0.1117	0.66 + 0.94i	6	4.35	5.56
0.3325	0.79 + 0.98i	6.35	4	4.49
1.1508	1.05 + 1.00i	7	3.47	12.26
1.9646	1.34 + 0.94i	7.65	3	4.44
2.4179	1.50 + 0.87i	8	2.74	16.42
3.4759	1.87 + 0.49i	8.72	2	4.12
4.0242	2.00 − 0.05i	8.85	1	3.85
3.8603	1.73 − 0.68i	8	1.56i	−22.26
3.4893	1.43 + 0.90i	7	2.13i	−23.74
3.1793	1.17 − 0.99i	6	2.49i	−21.14
2.9576	0.96 − 1.00i	5	2.76i	−17.57
2.8218	0.80 − 0.98i	4	2.96i	−14.19
2.7541	0.68 − 0.95i	3	3.09i	−11.41
2.7293	0.61 − 0.92i	2	3.14i	−9.32
2.7239	0.57 − 0.90i	1	3.15i	−8.00

with $d = 0.1$. For clarity of the figures, we did not include any secondary bifurcation branches, i.e., branches not directly coming off the trivial branch. A discussion of secondary bifurcation points is given in Appendix E. The analytical and numerical description of secondary bifurcations coming with the effect of period-doubling, -tripling etc. is provided in Ref. [29]. Let us mention that this phenomenon was discovered in earlier bifurcation analyses, cf. Refs. [24, Fig. 5] and [15, Fig. 10] for BSs and [20, Fig. 12] for DSs. We recall that in these studies the detuning was fixed and the forcing parameter was considered as a bifurcation parameter. The bifurcation branches in Fig. 1 were computed by the software `pde2path` (cf. Refs. [30,31]) which is designed to numerically treat continuation and bifurcation of PDE systems. Given a starting point on the trivial branch together with a tangent direction, `pde2path` starts a continuation algorithm to compute the trivial branch. Whenever a simple eigenvalue of the linearization crosses zero, a bifurcation point is detected and the bifurcating branch can be followed.

For the example given in Fig. 1(a), all calculated bifurcation points in Table I were reproduced by `pde2path`. Bifurcation branches determined by `pde2path` are shown in Fig. 1(a) as colored lines. Here, the single-soliton branch ($m = 1$) is highlighted in red. Blue branches are related to higher-order soliton frequency combs ($m = 2, \dots, 8$). Note that the bifurcation branches seem to stop at the points where a maximal value of ζ is reached. But, in fact, these points are turning points, and each branch continues in opposite directions on nearly the same path. A finer resolution of the turning of the branches reveals a snaking behavior shown in Fig. 4(b) in Appendix E. In Fig. 1(d), the same analysis is performed for normal dispersion ($d = -0.1$). The single-dark-soliton branch is again marked in red, higher-order soliton branches are marked in blue. Note that `pde2path` does not only generate the bifurcation map, but also allows us to calculate the stationary solutions of the LLE along the various branches.

Our choice of resonator length equals 2π in contrast to 100 in Ref. [24] and 160 in Refs. [15,20]. Rescaling the solutions from larger periodicities to 2π changes the dispersion from $|d| = 1$ in Refs. [15,20,24] to values of $|d| \approx 10^{-3}$, which is much smaller than our choice of $|d| = 0.1$. Notice that smaller dispersion parameters $|d|$ lead to a larger number of bifurcation points, cf. Ref. [21, Theorems 1.4 and 1.5], so it is to be expected that the diagrams in Refs. [15,20,24] show more bifurcation branches than shown here. Our choice of $f = 2$ is for illustrative purposes, so global features in Fig. 1 can be visualized more easily.

Complementing Fig. 1, we give further information on the connectedness of the branches as well as stability properties of solutions including those with multiple peaks in Appendix E. In the following, we will study the properties of the 1-solitons.

III. SOLITONS ALONG BIFURCATING BRANCHES

For a global study, we use `pde2path` to explore a much more extensive parameter space aiming at the detection of 1-soliton states on bifurcating branches. Based on a large number of numerical experiments, we developed heuristics that allow us to identify branches with single-soliton states and to find the solitons with the strongest spatial localization. Let us number the bifurcation points and bifurcating branches along $(\zeta, a_0(\zeta))$, starting from the left end of the trivial branch.

(i) For anomalous dispersion ($d > 0$), bright 1-solitons occur on the last bifurcating branch. The most localized 1-solitons occur near the first turning point of this branch (locally maximizing ζ). In Fig. 1(a), the corresponding branch is labeled $m = 1$. It contains the solutions A,B,C that are illustrated with regard to the spatial and spectral power distribution in Figs. 1(b) and 1(c), respectively. The first turning point is indicated by C.

(ii) For normal dispersion ($d < 0$), dark 1-solitons occur on the first bifurcating branch. The most localized 1-solitons occur near the second turning point of this branch (locally maximizing ζ). In Fig. 1(d), the corresponding branch contains the solutions D,E,F that are illustrated with regard to the spatial and spectral power distribution in Figs. 1(e) and 1(f), respectively. The second turning point is indicated by F.

These heuristics are illustrated in Fig. 2, where the full width at half maximum (FWHM_a) in case of BSs as well as the full width at half minimum (FWHM_i) in the case of DSs are plotted for the spatial field distribution along the bifurcating branch starting from the initial bifurcation point. Note that the bright 1-soliton at point C in Fig. 1(a) has slightly smaller $\mathrm{FWHM}_a = 0.3330$ than the bright 1-soliton at point B ($\mathrm{FWHM}_a = 0.3393$). Both for normal and anomalous dispersion, the common feature of the most localized 1-solitons is their occurrence at maximal detuning values within all turning points of the bifurcating branch. These heuristics are illustrated in Fig. 1. For different points A, B,

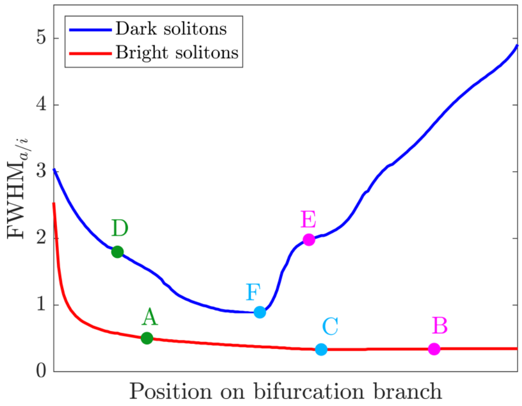

FIG. 2. Full width at half maximum (FWHM_a) of bright solitons along the bifurcating branch for anomalous dispersion (red, $d = 0.1$) and full width at half minimum (FWHM_i) of dark solitons for normal dispersion (blue, $d = -0.1$) for $f = 2$. Horizontal axis shows normalized arc length along bifurcation branches. Quantities on both axes are dimensionless.

C along the bright-single-soliton branch and D, E, F along the dark-single-soliton branch, respectively, comb states are depicted in the spatial and frequency domain in Figs. 1(b), 1(c), 1(e), and 1(f). As expected, the comb states with the smallest $\mathrm{FWHM}_{a/i}$ identified in points C and F by using the aforementioned heuristics show the strongest localization in the spatial domain. Furthermore, we can see that in the case of anomalous dispersion, there is no other state on the branch $m = 1$ for the same value of ζ. However, in the case of normal dispersion, we find another DS state with equal detuning marked by point D in Fig. 1(d), cf. Ref. [14]. Yet point F in Fig. 1(d) shows a stronger spatial localization, cf. Fig. 2, and has a broader frequency comb than D.

In this example, the soliton character of the solutions, i.e., their strong localization in the spatial domain at the turning point is visible but not yet very pronounced due to the moderate value of f. With increasing f, the soliton localization as well as the comb power and comb bandwidth will be much enhanced. At the same time, the graphs of the bifurcation branches will be less illustrative due to a steeply increasing number and density of bifurcation points. Therefore, $f = 2$ is chosen merely for illustrative reasons, and much larger ranges of f are covered in Sec. IV.

IV. QUANTITATIVE CHARACTERIZATION OF SOLITON FREQUENCY COMBS

Using the heuristics from the previous section, we are able to identify single-soliton states with the strongest spatial localization for any fixed forcing both in the normal as well as anomalous-dispersion regime. Based on this approach, we now characterize these comb states $a(x) = \sum_{k\in\mathbb{Z}} \hat{a}_k e^{ikx}$ by their comb bandwidth $2k^\star$ and their power conversion efficiency (PCE) η. The comb bandwidth is quantified by the 3dB point, i.e., by the minimal integer $k^\star$ that fulfills $|\hat{a}_{k^\star}|^2 \leqslant \frac{1}{2}|\hat{a}_1|^2$. Note that the 3dB comb bandwidth is defined with respect to the power $|\hat{a}_1|^2$ of the mode directly adjacent to the pumped mode rather than the power $|\hat{a}_0|^2$ of the pumped mode itself, which is usually much stronger than all other modes of the comb. The PCE is the ratio between the intracavity comb power

$$P_{\mathrm{FC}} = \sum_{k\in\mathbb{Z}\setminus\{0\}} |\hat{a}_k|^2 \tag{8}$$

and the pump power f^2. Note that the intracavity comb power does not contain the zero mode, since $|\hat{a}_0|^2$ mostly stems from the pump and is therefore nonzero even if no comb is formed in the microresonator. For BSs, under the assumption of small damping and small forcing, approximation formulas for the comb bandwidth as well as the PCE exist, cf. Refs. [12,32–35]. Assuming a detuning set to the maximum value that permits a single soliton $\zeta_{\mathrm{BS,max}} = \pi^2 f^2/8$ [12,33], they read as follows:

$$2k^\star_{\mathrm{BS,max}} \approx \sqrt{2}\ln(1+\sqrt{2})\frac{f}{\sqrt{d}}, \tag{9a}$$

$$\eta_{\mathrm{BS,max}} \approx \frac{1}{f}\sqrt{\frac{d}{2}}. \tag{9b}$$

More details on these equations can be found in Appendix C. Expressions for the approximation of DSs resembling a flipped sech function on top of a cw background are given in Ref. [20]; compare the green curve in Fig. 1(e). They are valid near the bifurcation point and are obtained using multiple scale asymptotics. As mentioned before, these kind of solitons, indicated in Fig. 1(d) by point D, is of less interest due to its weaker localization, reduced comb bandwidth, and power compared to the DS at point F. For DSs of the latter type, no formula for the comb bandwidth or PCE is available, to the best of our knowledge.

For dispersion parameters $d = \pm 0.1, \pm 0.15, \pm 0.2, \pm 0.25$ and $f > 1$, we have carried out a large parameter study. For $d > 0$, we computed the last bifurcation point and its corresponding bifurcating branch. Based on the heuristics in Sec. III, we stopped the computation as soon as we reached the first turning point, i.e., point C in Fig. 1(a), where the most localized BS is found. In the same manner, the strongest localized DS in the case $d < 0$ is at the second turning point of the first bifurcating branch, i.e., point F in Fig. 1(d). For all of the above values of the dispersion d and the pump power f, the corresponding solitons at the turning point were investigated and their comb bandwidth as well as their PCE were evaluated.

The results are plotted in Fig. 3. For BSs, gray lines corresponding to the approximate expressions in Eqs. (9a) and (9b) are also shown in Figs. 3(a) and 3(c). As mentioned before, the validity of these approximations is guaranteed only for small damping, small forcing, and large forcing/damping ratio [34,35]. This explains the deviations from the curves computed by numerical bifurcation and continuation which occur for PCE in the small f regime [damping in Eq. (2) is set to 1] in Fig. 3(c) and for comb bandwidth in the large f regime in Fig. 3(a). The comb bandwidth increases with an increasing f at the expense of a decreasing conversion efficiency. Additionally, one can see that with $d \to 0$ the comb bandwidth increases whereas the PCE decreases.

For DSs, the overall dependence of the conversion efficiency and comb bandwidth shows the same trends as for

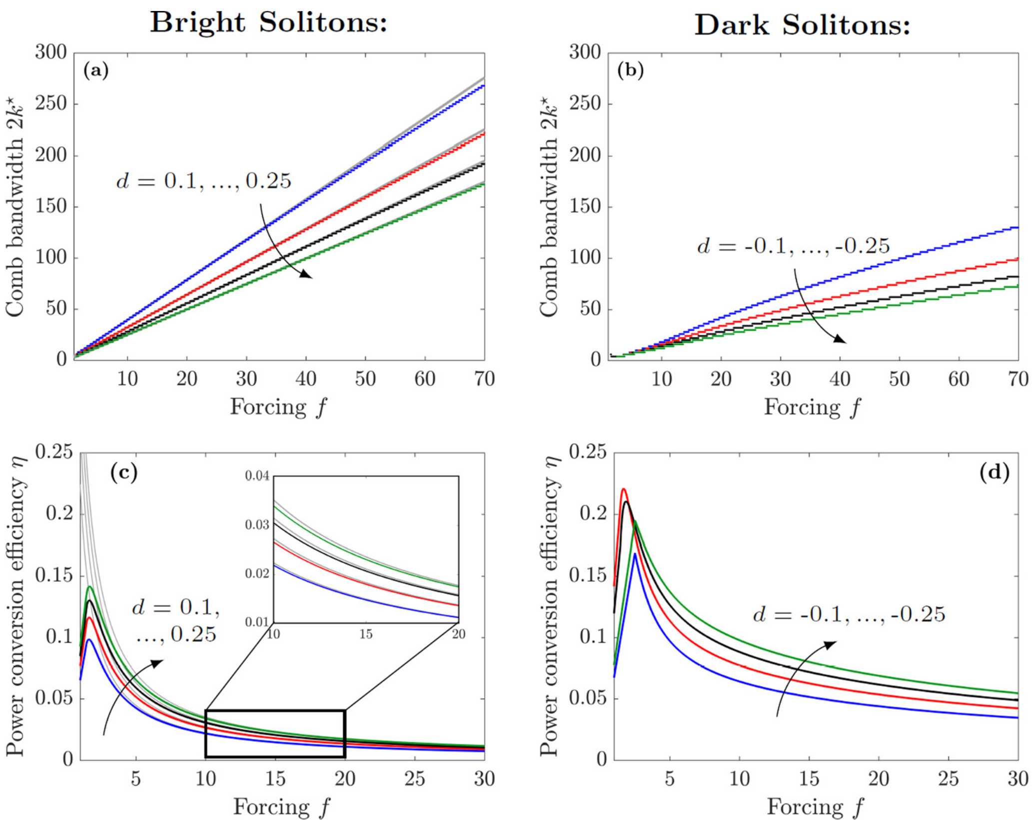

FIG. 3. Bandwidths $2k^\star$ and power conversion efficiencies (PCE) η for bright-soliton combs (a), (c) and dark-soliton combs (b), (d) as a function of the forcing f and dispersion $d = \pm 0.1, \pm 0.15, \pm 0.2, \pm 0.25$. Quantities on axes are dimensionless. (a) Bandwidth of bright-soliton combs obtained by numerical bifurcation and continuation (NBC, colored lines) along with an approximation according to Eq. (9a). The linear approximation is in good agreement with the numerical results and deviates only for a strong forcing. A stronger dispersion leads to a decreasing comb bandwidth. (b) Bandwidth of dark-soliton combs obtained by NBC. (c) PCE of bright-soliton states obtained by NBC (colored lines) along with an approximation according to Eq. (9b) (gray lines). The approximation is in good agreement with the numerical results, but deviates strongly for weak forcing. A weaker dispersion leads to a decreasing PCE. (d) PCE of dark-soliton states obtained by NBC. The PCE decreases with an increasing forcing, but is overall higher as for bright solitons. Here, weaker dispersion also leads to a decreasing PCE.

BSs, see Figs. 3(b) and 3(d). In direct comparison, DSs have a decreased bandwidth along with a higher conversion efficiency for the same values of f and $|d|$. We attribute this to the strong constant background of the DSs in the spatial domain which enables a more efficient power transfer from the CW pump to the soliton. However, the increased spatial width of the DSs is also linked to a narrower frequency comb in the spectral domain. We note that the comb bandwidth of both BSs and DSs does not increase strictly linearly with an increasing forcing. For DSs, the nonlinear behavior is more pronounced.

For the physical properties of soliton frequency combs in non-normalized units, the bandwidth $2k^\star$ as well as the conversion efficiency η have to be converted. The physical comb bandwidth $\Delta\omega/(2\pi)$ is obtained by multiplying $2k^\star$ with the free spectral range FSR of the resonator, i.e., the inverse of the roundtrip time T_R of the light inside:

$$\Delta\omega/(2\pi) = \text{FSR} \times 2k^\star = T_R^{-1} \times 2k^\star. \tag{10}$$

To determine the physical conversion efficiency outside the resonator η_{out}, the physical power coupling coefficient κ between the bus waveguide and the microresonator as well as the physical roundtrip-power-loss coefficient α have to be taken into consideration via the relation

$$\eta_{\text{out}} = \frac{4\kappa^2}{(\alpha+\kappa)^2}\eta. \tag{11}$$

For details on Eq. (11), see Appendix D. To achieve high external power conversion efficiencies >30% as, e.g., in Ref. [36], an *overcoupled* resonator with $\alpha \ll \kappa$ is preferable. As visible in Figs. 3(c) and 3(d), a microresonator with normal dispersion-enabling DS states will tend to improve the PCE. It should be noted, however, that the generation of normal-dispersion frequency combs generally requires an avoided mode crossing for initial modulation instability [26], which makes the design of the device more complex.

V. SUMMARY

We have performed a global bifurcation analysis of the LLE and provided an overview on the structure of nontrivial solutions. We find single-soliton frequency combs both in the normal and anomalous-dispersion regime. Our investigation covers a broad space of technically relevant device and operation parameters. It allows us to identify the broadest soliton combs and to benchmark them with respect to bandwidth and pump-to-comb power conversion efficiency. Our findings are in good agreement with simplified analytic models. Comparing the results for BSs and DSs, we find that DSs outperform BSs significantly in terms of power conversion efficiency at the expense of a reduced bandwidth.

The bifurcation and continuation method allows us to determine the performance parameters of single-soliton comb states even for the cases where simplified analytic models are not valid, e.g., for certain DSs. Our approach can be further extended to include additional effects such as two-photon absorption and to study their impact on the stationary comb states, see Ref. [37]. The results of our investigation allow for targeted design of soliton comb generators for specific applications. In this context, the power conversion efficiency and the comb bandwidth are key performance characteristics that need to be optimized under technical restrictions such as limited optical input power.

ACKNOWLEDGMENT

Funded by the Deutsche Forschungsgemeinschaft (DFG, German Research Foundation) Project-ID 258734477 - SFB 1173

APPENDIX A: IDENTIFICATION OF BIFURCATION POINTS

Here we derive the expression that allows us to identify bifurcation points on the curve of trivial solutions to the stationary LLE with Neumann boundary conditions:

$$-da'' - (\mathrm{i} - \zeta)a - |a|^2 a + \mathrm{i}f = 0, \tag{A1}$$

$$a'(0) = a'(\pi) = 0. \tag{A2}$$

The structure of the solutions $a : [0,\pi] \to \mathbb{C}$ near a point $(\zeta_0, a_0(\zeta_0))$ on the trivial curve depends on the properties of the linearized operator L

$$L\phi : = -d\phi'' - (\mathrm{i} - \zeta_0)\phi - 2|a_0|^2\phi - a_0^2\bar{\phi}, \tag{A3a}$$

$$\phi'(0) = \phi'(\pi) = 0, \tag{A3b}$$

where we write a_0 instead of $a_0(\zeta_0)$, but we keep the notation $a_0(\zeta)$ whenever we want to stress the ζ-dependence of the trivial solution. We denote the kernel of the differential operator L by $\operatorname{Ker} L = \{\phi : L\phi = 0, \phi'(0) = \phi'(\pi) = 0\}$ and its range by $\operatorname{Rg} L = \{L\phi : \phi'(0) = \phi'(\pi) = 0\}$, where the functions $\phi : [0,\pi] \to \mathbb{C}$ are twice continuously differentiable. For such a function $\phi \neq 0$, we denote by $\operatorname{span}\{\phi\} = \{t\phi : t \in \mathbb{R}\}$ the one-dimensional space of all real multiples of ϕ and by $\operatorname{span}\{\phi\}^{\perp} = \{\psi : \int_0^{\pi} \phi(x)\bar{\psi}(x)\,dx = 0\}$ its L^2-orthogonal complement. Let us abbreviate the nonlinearity in Eq. (A1) by $g(a) = |a|^2 a - \mathrm{i}f$. The derivative $Dg(a)z := \frac{d}{dt} g(a + tz)|_{t=0} = 2|a|^2 z + a^2\bar{z}$ for $a, z \in \mathbb{C}$ appeared in Eq. (A3) in the definition of the linearized operator L. It can also be written in the form

$$Dg(a)z = \begin{pmatrix} 3(\operatorname{Re} a)^2 + (\operatorname{Im} a)^2 & 2\operatorname{Re} a \operatorname{Im} a \\ 2\operatorname{Re} a \operatorname{Im} a & (\operatorname{Re} a)^2 + 3(\operatorname{Im} a)^2 \end{pmatrix} \begin{pmatrix} \operatorname{Re} z \\ \operatorname{Im} z \end{pmatrix}. \tag{A4}$$

Besides the linearized operator L given in Eq. (A3), we also consider its adjoint operator,

$$L^*\phi = -d\frac{d^2}{dx^2}\phi + (\mathrm{i} + \zeta_0)\phi - \overline{Dg(a_0(\zeta_0))}\phi, \tag{A5a}$$

$$\phi'(0) = \phi'(\pi) = 0, \tag{A5b}$$

which will be used below. Next we will compute the spaces $\operatorname{Ker} L$, $\operatorname{Ker} L^*$, which have the same finite dimension since both L and L^* are Fredholm operators. Owing to the Neumann boundary conditions, any element $\phi \in \operatorname{Ker} L$ can be expanded in the form $\phi(x) = \sum_{l=0}^{\infty} \alpha_l \cos(lx)$. Since $\{\cos(lx)\}_{l\in\mathbb{N}_0}$ is a basis and L is linear the condition that $\phi \in \operatorname{Ker} L$ means that there is at least one integer $k \in \mathbb{N}_0$ such that $L(\alpha\cos(kx)) = (dk^2 - \mathrm{i} + \zeta_0 - Dg(a_0))\alpha\cos(kx) = 0$ for some $\alpha = (\operatorname{Re}\alpha, \operatorname{Im}\alpha) \in \mathbb{C} \setminus \{0\}$. Using Eq. (A4), it follows that dk^2 must be an eigenvalue of the matrix

$$N = \begin{pmatrix} -\zeta_0 + 3(\operatorname{Re} a_0)^2 + (\operatorname{Im} a_0)^2 & 2\operatorname{Re} a_0 \operatorname{Im} a_0 - 1 \\ 2\operatorname{Re} a_0 \operatorname{Im} a_0 + 1 & -\zeta_0 + (\operatorname{Re} a_0)^2 + 3(\operatorname{Im} a_0)^2 \end{pmatrix}, \tag{A6}$$

with eigenvector α. Nonzero elements in $\operatorname{Ker} L$ exist if $\det(-dk^2\,\mathrm{Id} + N) = 0$ and computing this determinant yields

$$(\zeta_0 + dk^2)^2 - 4|a_0(\zeta_0)|^2(\zeta_0 + dk^2) + 1 + 3|a_0(\zeta_0)|^4 = 0. \tag{A7}$$

Solving for k leads to $k_{1,2}$, given by the following equation:

$$k_{1,2} := \sqrt{\frac{2|a_0(\zeta_0)|^2 - \zeta_0 \pm \sqrt{|a_0(\zeta_0)|^4 - 1}}{d}}. \tag{A8}$$

Likewise, nonzero elements in $\operatorname{Ker} L^*$ exist if $\det(-d\tilde{k}^2\,\mathrm{Id} + N^T) = 0$ for some integer $\tilde{k} \in \mathbb{N}_0$. Since $\det(-d\tilde{k}^2\,\mathrm{Id} + N^T) = \det(-d\tilde{k}^2\,\mathrm{Id} + N)$, this leads to the same formula Eq. (A8) for $\tilde{k}_{1,2}$. In the remaining part of this section, we write k as a shorthand for one of the two values $k_{1,2}$. Consequently, under the condition from Eq. (A7) there is a vector α and a vector α^* such that $\alpha\cos(kx) \in \operatorname{Ker} L$ and $\alpha^*\cos(kx) \in \operatorname{Ker} L^*$.

Now we determine α and α^* under the condition from Eq. (A7). In the matrix $N - dk^2\,\mathrm{Id}$, the first or the second line could be zero (but not both). Therefore, the eigenvector α of the matrix in Eq. (A6) is given in the form

$$\alpha = \begin{pmatrix} 2\operatorname{Re} a_0 \operatorname{Im} a_0 - 1 \\ \zeta + dk^2 - 3(\operatorname{Re} a_0)^2 - (\operatorname{Im} a_0)^2 \end{pmatrix} \text{ or}$$

$$\alpha = \begin{pmatrix} \zeta + dk^2 - (\operatorname{Re} a_0)^2 - 3(\operatorname{Im} a_0)^2 \\ 2\operatorname{Re} a_0 \operatorname{Im} a_0 + 1 \end{pmatrix}, \tag{A9}$$

such that $(-dk^2\,\mathrm{Id} + N)\alpha = 0$, and hence $\alpha\cos(kx)$ belongs to $\operatorname{Ker} L$. The first choice can be taken if $2\operatorname{Re} a_0 \operatorname{Im} a_0 - 1 \neq 0$ and the second choice if $2\operatorname{Re} a_0 \operatorname{Im} a_0 + 1 \neq 0$. Likewise,

$$\alpha^* = \begin{pmatrix} \zeta + dk^2 - (\operatorname{Re} a_0)^2 - 3(\operatorname{Im} a_0)^2 \\ 2\operatorname{Re} a_0 \operatorname{Im} a_0 - 1 \end{pmatrix} \text{ or}$$

$$\alpha^* = \begin{pmatrix} 2\operatorname{Re} a_0 \operatorname{Im} a_0 + 1 \\ \zeta + dk^2 - 3(\operatorname{Re} a_0)^2 - (\operatorname{Im} a_0)^2 \end{pmatrix} \tag{A10}$$

with $\alpha^* = (\operatorname{Re}\alpha^*, \operatorname{Im}\alpha^*) \in \mathbb{C}$ satisfies $(-dk^2\,\mathrm{Id} + N^T)\alpha^* = 0$ and leads to an element $\alpha^*\cos(kx) \in \operatorname{Ker} L^*$. As before, the first choice can be taken if $2\operatorname{Re} a_0 \operatorname{Im} a_0 - 1 \neq 0$ and the second choice if $2\operatorname{Re} a_0 \operatorname{Im} a_0 + 1 \neq 0$.

We can exclude the case $k_1 = 0$ or $k_2 = 0$ in the bifurcation condition from Eq. (A7) since it would only lead to bifurcation of trivial solutions, and we are interested in nontrivial solutions. The kernel of L will be one-dimensional provided that in Eq. (A7) we have $k_1 \in \mathbb{N}$ and $k_2 \notin \mathbb{N}$ or vice versa, and two-dimensional if both $k_1, k_2 \in \mathbb{N}$. If neither k_1 or k_2 are in $\mathbb{N}$, then $\operatorname{Ker} L = \operatorname{Ker} L^* = \{0\}$, and the implicit function theorem (cf. Ref. [27, Theorem I.1.1]) implies that solutions nearby the point (ζ_0, a_0) are unique, and therefore trivial. Hence, (ζ_0, a_0) cannot be a bifurcation point in this case, and therefore the necessary bifurcation condition is that $k_1 \in \mathbb{N}$ or $k_2 \in \mathbb{N}$. The same condition, expressed in the form of Eq. (A7), is given in Ref. [21, Proposition 10].

APPENDIX B: TRANSVERSALITY CONDITION

According to the Crandall-Rabinowitz theorem (cf. Refs. [38, Theorem I.5.1] and [27]), two conditions are sufficient for bifurcation. The first is that $\operatorname{Ker} L$ is one-dimensional, i.e., with k_1, k_2 from Eq. (A8), we need that $k_1 \in \mathbb{N}, k_2 \notin \mathbb{N}$ or vice versa, and we write k for the one which is the integer. As we will see, the second condition (the transversality condition) is given by

$$\begin{aligned}&2|a_0(\zeta_0)|^4(|a_0(\zeta_0)|^2 - \zeta_0)\\ &\quad\mp (1 + \zeta_0^2 - |a_0(\zeta_0)|^4)\sqrt{|a_0(\zeta_0)|^4 - 1} \neq 0 \qquad \text{(B1)}\end{aligned}$$

with $-$ if $k_1 \in \mathbb{N}$ and $+$ if $k_2 \in \mathbb{N}$. To verify that Eq. (B1) together with the one-dimensionality of the kernel is really sufficient for bifurcation, we need to bring our problem into the form used in Ref. [38]. Nontrivial solutions of Eqs. (A1) and (A2) may be written as $a(x) = a_0(\zeta) + b(x)$ with $b'(0) = b'(\pi) = 0$. From Eqs. (A1) and (A2), we derive the equation for the function b in the form

$$F(\zeta, b) := -db'' - (\mathrm{i} - \zeta)(a_0(\zeta) + b) - g(a_0(\zeta) + b) = 0, \qquad \text{(B2)}$$

where F is defined on $\mathbb{R} \times H$ with H given as the real Hilbert space of twice almost everywhere differentiable functions $b : [0, \pi] \to \mathbb{C}$ with $b'(0) = b'(\pi) = 0$ and b, b'' being square integrable. Notice that $F(\zeta, 0) = 0$ for all ζ, i.e., the curve of trivial solutions $(\zeta, a_0(\zeta))$ for Eqs. (A1) and (A2) has now become the line of zero solutions $(\zeta, 0)$ for Eq. (B2). Let us write $D^2_{b,\zeta}F(\zeta_0, 0)$ for the mixed second derivative of F with respect to b and ζ at the point $(\zeta_0, 0)$. In our case, where F is defined by Eq. (B2), we find for the mixed second derivative

$$\begin{aligned}D^2_{b,\zeta}F(\zeta_0, 0)\phi &= \phi - D^2 g(a_0)(\phi, \dot{a}_0)\\ &= \phi - 2\bar{a}_0\phi\dot{a}_0 - 2a_0\phi\overline{\dot{a}_0} - 2a_0\bar{\phi}\dot{a}_0, \qquad \text{(B3)}\end{aligned}$$

where $\dot{a}_0 = \frac{d}{d\zeta}a_0(\zeta)|_{\zeta=\zeta_0}$ is the tangent direction along the curve $\zeta \mapsto a_0(\zeta)$ at the point ζ_0. According to Ref. [38], the transversality condition is expressed by

$$D^2_{b,\zeta}F(\zeta_0, 0)\phi \notin \operatorname{Rg}(D_b F(\zeta_0, 0)),$$

with ϕ such that $\operatorname{Ker}(D_b F(\zeta_0, 0)) = \operatorname{span}\{\phi\}$. In our case, $D_b F(\zeta_0, 0) = L$, where L is the linearized operator given in Eq. (A3). By the Fredholm alternative, cf. Ref. [39], $\operatorname{Rg} L = (\operatorname{Ker} L^*)^\perp = \operatorname{span}\{\phi^*\}^\perp$, where $\phi(x) = \alpha\cos(kx)$, $\phi^*(x) = \alpha^*\cos(kx)$ with α from Eqs. (A9) and α^* from Eqs. (A10). Here orthogonality $u \perp v$ of two functions $u, v \in H$ is understood as vanishing of the inner product $\langle u, v\rangle = \operatorname{Re}\int_0^\pi u(x)\bar{v}(x)\,dx$. Hence, transversality is expressed as

$$\left\langle D^2_{b,\zeta}F(\zeta_0, 0)\phi, \phi^*\right\rangle = \operatorname{Re}\int_0^\pi \left(D^2_{b,\zeta}F(\zeta_0, 0)\phi\right)\overline{\phi^*}\,dx \neq 0, \qquad \text{(B4)}$$

and we will show next that this amounts to

$$\begin{aligned}\left\langle D^2_{b,\zeta}F(\zeta_0, 0)\phi, \phi^*\right\rangle = &\frac{-\pi(2\operatorname{Re} a_0 \operatorname{Im} a_0 \mp 1)}{3|a_0|^4 - 4|a_0|^2\zeta_0 + \zeta_0^2 + 1}\\ &\times \Big((dk^2 - \zeta_0)|a_0|^4\\ &\quad + \big(\zeta_0^2 + 1\big)(2|a_0|^2 - dk^2 - \zeta_0)\Big). \qquad \text{(B5)}\end{aligned}$$

To evaluate $D^2_{b,\zeta}F(\zeta_0, 0)\phi$, we first need to determine the tangent $\dot{a}_0 = \frac{d}{d\zeta}a_0(\zeta)|_{\zeta=\zeta_0}$. Differentiating the equation $(\mathrm{i} - \zeta)a_0(\zeta) + g(a_0(\zeta)) = 0$ with respect to ζ and evaluating the derivative at ζ_0, we get

$$(Dg(a_0) + \mathrm{i} - \zeta_0)\dot{a}_0 = a_0.$$

Recalling that $Dg(a_0)z = 2|a_0|^2 z + a_0^2\bar{z}$, we thus find

$$(2|a_0|^2 + \mathrm{i} - \zeta_0)\dot{a}_0 + a_0^2\overline{\dot{a}_0} = a_0$$

and hence

$$\dot{a}_0 = \tau a_0 \quad \text{with} \quad \tau = \frac{|a_0|^2 - \zeta_0 - \mathrm{i}}{3|a_0|^4 - 4|a_0|^2\zeta_0 + \zeta_0^2 + 1}. \qquad \text{(B6)}$$

Inserting $\dot{a}_0$ from Eq. (B6) into Eq. (B3), we deduce that the transversality condition Eq. (B4) becomes

$$\begin{aligned}&\left\langle D^2_{b,\zeta}F(\zeta_0, 0)\phi, \phi^*\right\rangle\\ &\quad = \frac{\pi}{2}\operatorname{Re}\left(\alpha\overline{\alpha^*} - 4\operatorname{Re}\tau|a_0|^2\alpha\overline{\alpha^*} - 2\tau a_0^2\bar{\alpha}\overline{\alpha^*}\right) \neq 0. \qquad \text{(B7)}\end{aligned}$$

Depending on the alternatives in Eqs. (A9) and (A10) for the actual form of α, α^*, we obtain

$$\operatorname{Re}\alpha\overline{\alpha^*} = (2\operatorname{Re} a_0 \operatorname{Im} a_0 \mp 1)(2\zeta_0 + 2dk^2 - 4|a_0|^2).$$

Likewise,

$$\begin{aligned}\bar{\alpha}\overline{\alpha^*} = &(2\operatorname{Re} a_0 \operatorname{Im} a_0 \mp 1)(\zeta_0 + dk^2 - (\operatorname{Re} a_0)^2 - 3(\operatorname{Im} a_0)^2) - (2\operatorname{Re} a_0 \operatorname{Im} a_0 \mp 1)(\zeta_0 + dk^2 - 3(\operatorname{Re} a_0)^2 - (\operatorname{Im} a_0)^2)\\ &- \mathrm{i}\Big((2\operatorname{Re} a_0 \operatorname{Im} a_0 \mp 1)^2 + \underbrace{(\zeta_0 + dk^2 - 3(\operatorname{Re} a_0)^2 - (\operatorname{Im} a_0)^2)(\zeta_0 + dk^2 - (\operatorname{Re} a_0)^2 - 3(\operatorname{Im} a_0)^2)}_{\overset{(A7)}{=}4(\operatorname{Re} a_0)^2\operatorname{Im}(a_0)^2 - 1}\Big)\\ &= (2\operatorname{Re} a_0 \operatorname{Im} a_0 \mp 1)2\bar{a}_0^2,\end{aligned}$$

where we have used the necessary bifurcation condition from Eq. (A7). Taking the expressions for $\operatorname{Re}\alpha\overline{\alpha^*}$ and $a_0^2\bar{\alpha}\overline{\alpha^*}$ into the transversality condition from Eq. (B7) finally leads to

$$\begin{aligned}
&\left\langle D^2_{b,\zeta}F(\zeta_0,0)\phi,\phi^*\right\rangle\\
&\quad=\frac{\pi}{2}\operatorname{Re}\left(\alpha\overline{\alpha^*}-4\operatorname{Re}\tau|a_0|^2\alpha\overline{\alpha^*}-2\tau a_0^2\bar{\alpha}\overline{\alpha^*}\right)\\
&\quad=\frac{\pi}{2}(2\operatorname{Re}a_0\operatorname{Im}a_0\mp 1)((2\zeta_0+2dk^2-4|a_0|^2)\\
&\qquad\times\ (1-4\operatorname{Re}\tau|a_0|^2)-4\operatorname{Re}\tau|a_0|^4)\neq 0.
\end{aligned}$$

Since the choices in Eqs. (A9) and (A10) were made so the factor $(2\operatorname{Re}a_0\operatorname{Im}a_0\mp 1)$ is nonzero, the nonvanishing of the expression in brackets amounts to (after inserting $\operatorname{Re}\tau=\frac{|a_0|^2-\zeta_0}{3|a_0|^4-4|a_0|^2\zeta_0+\zeta_0^2+1}$)

$$(dk^2-\zeta_0)|a_0|^4+\left(\zeta_0^2+1\right)(2|a_0|^2-dk^2-\zeta_0)\neq 0.$$

We have therefore verified Eq. (B5), and using the definition k_1, k_2 from Eq. (A8), we obtain the transversality condition in its final form Eq. (B1), where only a_0 and ζ_0 appear.

APPENDIX C: APPROXIMATIONS FOR THE BRIGHT-SOLITON POWER CONVERSION EFFICIENCY $\eta_{\mathrm{BS,max}}$ AND COMB BANDWIDTH $2k^{\star}_{\mathrm{BS,max}}$

For BSs, a closed form approximation [12,32–35] of the intracavity field is given by

$$a(x)\approx\Psi_0+\Psi_1(x)=\Psi_0+Be^{i\varphi_0}\operatorname{sech}\left(\frac{B}{\sqrt{2d}}x\right).\tag{C1}$$

Here, $\Psi_1(x)$ represents the field of a BS on top of a constant background field Ψ_0, $B\approx\sqrt{2\zeta}$ defines the width and the amplitude of the soliton, and $\varphi_0=\arccos\left(\frac{\sqrt{8\zeta}}{\pi f}\right)$ is the relative phase of the soliton with respect to Ψ_0. For strong solitons, the intracavity field will be dominated by the soliton itself, such that $a(x)\approx\Psi_1(x)$. For a given forcing, the maximum detuning can be derived by the condition that the argument of the arccos function may not exceed 1, cf. supplementary information in Ref. [12]. With maximum detuning $\zeta_{\max}=\frac{\pi^2 f^2}{8}$, $\varphi_0=0$, we find that the intracavity field reads

$$a(x)\approx\frac{\pi f}{2}\operatorname{sech}\left(\frac{\pi f}{2\sqrt{2d}}x\right).\tag{C2}$$

Given this expression, the power conversion efficiency at the maximum detuning for BSs can be computed by an integral in the spatial domain:

$$\begin{aligned}
\eta_{\mathrm{BS,max}}&=\frac{\frac{1}{2\pi}\int_{-\pi}^{\pi}\left|\frac{\pi f}{2}\operatorname{sech}\left(\frac{\pi f}{2\sqrt{2d}}x\right)\right|^2dx}{f^2}\\
&=\frac{1}{f}\sqrt{\frac{d}{2}}\tanh\left(\frac{\pi f}{2\sqrt{2d}}\pi\right)\approx\frac{1}{f}\sqrt{\frac{d}{2}}.
\end{aligned}\tag{C3}$$

To determine the comb bandwidth, we calculate the Fourier coefficients associated with the various comb lines. The power spectrum is given by the magnitude square of these coefficients:

$$\begin{aligned}
|\hat{a}_k|^2&=\left|\frac{1}{2\pi}\int_{-\pi}^{\pi}\frac{\pi f}{2}\operatorname{sech}\left(\frac{\pi f}{2\sqrt{2d}}x\right)e^{-ikx}\,dx\right|^2\\
&\approx\left|\frac{1}{2\pi}\int_{-\infty}^{\infty}\frac{\pi f}{2}\operatorname{sech}\left(\frac{\pi f}{2\sqrt{2d}}x\right)e^{-ikx}\,dx\right|^2\\
&=\frac{d}{2}\operatorname{sech}^2\left(\frac{\sqrt{2d}}{f}k\right).
\end{aligned}\tag{C4}$$

The (FWHM$_a$) bandwidth x_{FWHM} of the sech^2 function is given by the condition

$$\operatorname{sech}^2\left(\frac{x_{\mathrm{FWHM}}}{2}\right)=\frac{1}{2},\tag{C5}$$

which leads to $x_{\mathrm{FWHM}}=2\ln(1+\sqrt{2})$. This leads to the FWHM bandwidth $2k^{\star}_{\mathrm{BS,max}}$,

$$2k^{\star}_{\mathrm{BS,max}}=\frac{f}{\sqrt{2d}}x_{\mathrm{FWHM}}=\sqrt{2}\ln(1+\sqrt{2})\frac{f}{\sqrt{d}}.\tag{C6}$$

For a representation of the Eqs. (C3) and (C6) in physical, i.e., non-normalized units, see, e.g., Refs. [32,33].

APPENDIX D: PHYSICAL POWER CONVERSION EFFICIENCY OUTSIDE OF THE MICRORESONATOR

In physical terms, the time-dependent LLE [40] is given by

$$\begin{aligned}
T_R\frac{\partial E(T,\tau)}{\partial T}&=\sqrt{\kappa}\sqrt{P_{\mathrm{in}}}+\left(-\frac{\alpha}{2}-\frac{\kappa}{2}-\mathrm{i}\delta_0-\mathrm{i}\frac{\beta_2}{2}L\frac{\partial^2}{\partial\tau^2}\right.\\
&\quad\left.+\,\mathrm{i}\gamma L|E(T,\tau)|^2\right)E(T,\tau).
\end{aligned}\tag{D1}$$

Here, T_R is the roundtrip time of light circulating in the resonator, E the electric field, T the physical time, τ the roundtrip position inside the resonator, κ the power-coupling coefficient of the bus waveguide and the microresonator, P_{in} the power of the pump light, α the power roundtrip loss, β_2 the second order dispersion coefficient, L the circumference, and γ the nonlinearity coefficient of the microresonator. The detuning $\delta_0=(\omega_r-\omega_p)T_R$ is defined by the difference between the angular frequency of the pump laser ω_p, the angular resonance frequency ω_r and the round-trip time.

The normalized field $a(t,x)$ for $x\in[0,2\pi)$ and the normalized quantities ζ and d satisfy the time-dependent normalized LLE,

$$\frac{\partial a(t,x)}{\partial t}=f+\left(-1-\mathrm{i}\zeta+\mathrm{i}d\frac{\partial^2}{\partial x^2}+\mathrm{i}|a(t,x)|^2\right)a(t,x),$$

and are related to the physical parameters E and P_{in}, γ, α, κ, δ_0, T_R, and β_2 via

$$a(t,x)=\sqrt{\frac{2\gamma L}{\alpha+\kappa}}E(T,\tau),\tag{D2}$$

$$t=\frac{\alpha+\kappa}{2}\frac{T}{T_R},\tag{D3}$$

$$x=\frac{2\pi}{T_R}\tau,\tag{D4}$$

$$f = \sqrt{\frac{2\gamma L}{\alpha+\kappa}\frac{2\sqrt{\kappa}}{\alpha+\kappa}}\sqrt{P_{\text{in}}}, \tag{D5}$$

$$\zeta = \frac{2\delta_0}{\alpha+\kappa}, \tag{D6}$$

$$d = \frac{-4\pi^2\beta_2 L}{(\alpha+\kappa)T_R^2}. \tag{D7}$$

For the field $E(T,\tau) = \sum_{k\in\mathbb{Z}} \hat{E}_k(T)e^{ik2\pi\tau/T_R}$, the intracavity-power is given by $\frac{1}{T_R}\int_0^{T_R}|E(T,\tau)|^2\,d\tau = \sum_{k\in\mathbb{Z}}|\hat{E}_k|^2$. The power of the frequency comb is defined as power of the intracavity-field excluding the pumped mode, $P_{\text{p,FC}} = \sum_{k\in\mathbb{Z}\setminus\{0\}}|\hat{E}_k|^2$. The pumped mode is excluded since it will have a nonzero value even if no frequency comb is formed. The physical power conversion efficiency η_{in} inside the microresonator can then be expressed as

$$\eta_{\text{in}} = \frac{P_{\text{p,FC}}}{P_{\text{in}}} = \frac{\sum_{k\in\mathbb{Z}\setminus\{0\}}|\hat{E}_k|^2}{P_{\text{in}}}. \tag{D8}$$

When the comb is coupled out of the microresonator, the field amplitude is decreased by the square root of the power-coupling coefficient κ. Therefore, the physical conversion efficiency with respect to the comb power outside of the resonator η_{out} is given by

$$\eta_{\text{out}} := \frac{\sum_{k\in\mathbb{Z}\setminus\{0\}}|\sqrt{\kappa}\hat{E}_k|^2}{P_{\text{in}}} = \kappa\eta_{\text{in}}. \tag{D9}$$

Given the relations from Eqs. (D2) and (D5), the normalized power conversion efficiency η defined as the ratio between the power of the normalized frequency comb $\sum_{k\in\mathbb{Z}\setminus\{0\}}|\hat{a}_k|^2$ and the normalized forcing power f^2 can be expressed by physical quantities as follows:

$$\begin{aligned}\eta &= \frac{\sum_{k\in\mathbb{Z}\setminus\{0\}}|\hat{a}_k|^2}{f^2} = \frac{\sum_{k\in\mathbb{Z}\setminus\{0\}}\left|\sqrt{\frac{2\gamma L}{\alpha+\kappa}}\hat{E}_k\right|^2}{\left(\sqrt{\frac{2\gamma L}{\alpha+\kappa}\frac{2\sqrt{\kappa}}{\alpha+\kappa}}\sqrt{P_{\text{in}}}\right)^2}\\ &= \frac{(\alpha+\kappa)^2}{4\kappa}\eta_{\text{in}} = \frac{(\alpha+\kappa)^2}{4\kappa^2}\eta_{\text{out}}.\end{aligned} \tag{D10}$$

This is equivalent to Eq. (11) of the main paper.

APPENDIX E: BIFURCATION MAPS, STABILITY, AND MULTI-PEAK SOLUTIONS

In this Appendix, we explain and illustrate details on the global bifurcation maps of Figs. 1(a) and 1(d). In particular, we comment on the topics of *connectedness of branches, secondary bifurcations, and transition between soliton classes*, the use of a *different norm* to display certain aspects of the branches, and finally on the issue of *stability*.

1. Connectedness of branches, secondary bifurcations, and transition between soliton classes

At bifurcation points, branches of solutions intersect. Those bifurcation points that lie on the curve of constant solutions are called primary bifurcation points and they were described in Sec. II. Bifurcation points which are not lying on the curve of constant solutions are called secondary bifurcation points and they occur whenever two curves of nonconstant solutions join. In Figs. 4(a) (anomalous dispersion $d = 0.1$, forcing $f = 2$) and 5(a) (normal dispersion $d = -0.1$, forcing $f = 2$), we show which of the bifurcation curves are connected to each other by secondary bifurcations. Curves connected to each other by secondary bifurcations are plotted with the same color. Note that in a trivial sense all curves are connected to the curve of constant solutions via primary bifurcations—but these connections are not used for our coloring. All bifurcation points in Figs. 4(a) and 5(a) are marked as unfilled circles. The bifurcation points on the black curve of constant solutions are primary bifurcation points. Most secondary bifurcation points in Fig. 4(a) occur at turning points with the exception of one secondary bifurcation point that occurs on the blue curve near $\zeta = 0.8$. In Fig. 5(a), three secondary bifurcation points occur at $\zeta = 2.73$ (cf. zoom), $\zeta = 2.84$, and $\zeta = 3.36$.

Near secondary bifurcation points one can observe the transition between solutions of a different number of peaks, e.g., in the case of BSs in Fig. 4(b) a secondary bifurcation occurs at the turning point C'. Taking the 1-solitons at points A, C, B from Fig. 1(b) one can see their transition through U, V, W in Fig. 4(d) into equally spaced 2-solitons shown at Fig. 4(c) on the branch with A', C', B'. Following the branch A', C', B' further up, one finds another secondary bifurcation at a turning point where one meets the branch of 4-solitons. Similar observations can be made in the case of DSs. Fig. 5(a) and 5(b) show a secondary bifurcation near $\zeta = 3.36$. One can see how dark 1-solitons at points D, F, E known from Fig. 1(e) transform through X, Y, Z in Fig. 5(d) into equally spaced 2-solitons shown at Fig. 5(c) on the branch with D', F', E'. The state Z approximates a two soliton somewhere between F' and E'. We also show in the zoom of Fig. 5(a) how the curve of 1-solitons undergoes a secondary bifurcation with the curve of 3-solitons near $\zeta = 2.73$. Right after this bifurcation, the curves split up again. Since this happens close to the trivial curve, the visible effects on the solutions are marginal and are therefore not displayed.

Secondary bifurcations coming with the phenomenon period-doubling, -tripling etc. were found earlier in Refs. [15, Fig. 7(b)] or [24, Fig. 5] for anomalous dispersion and in Ref. [20, Fig. 12] for normal dispersion. An abstract result related to global secondary bifurcations with applications to Eqs. (2) and (3) can be found in Ref. [29].

2. Branches displayed in a different norm

In the case of anomalous dispersion, Fig. 4(a) shows the branches in the conventional norm $\|a\|_2^2$ which represents the intracavity power of the states. This norm does not capture well the fact that eight branches snake back and forth after having reached maximal values of ζ. In fact, comparing states on a fixed branch for the same value of ζ, one finds that the state obtained on the way out toward the maximal value of ζ is different compared with the state obtained on the way back. This effect can be visualized much better in Fig. 4(b), where instead of $\|a\|_2^2$ we use the norm

$$\|a - a_{av}\|_2^2 \text{ with } a_{av} := \frac{1}{2\pi}\int_0^{2\pi} a(x)\,dx$$

with the average value a_{av} being subtracted from a before the intracavity power measure is taken. This has the effect of

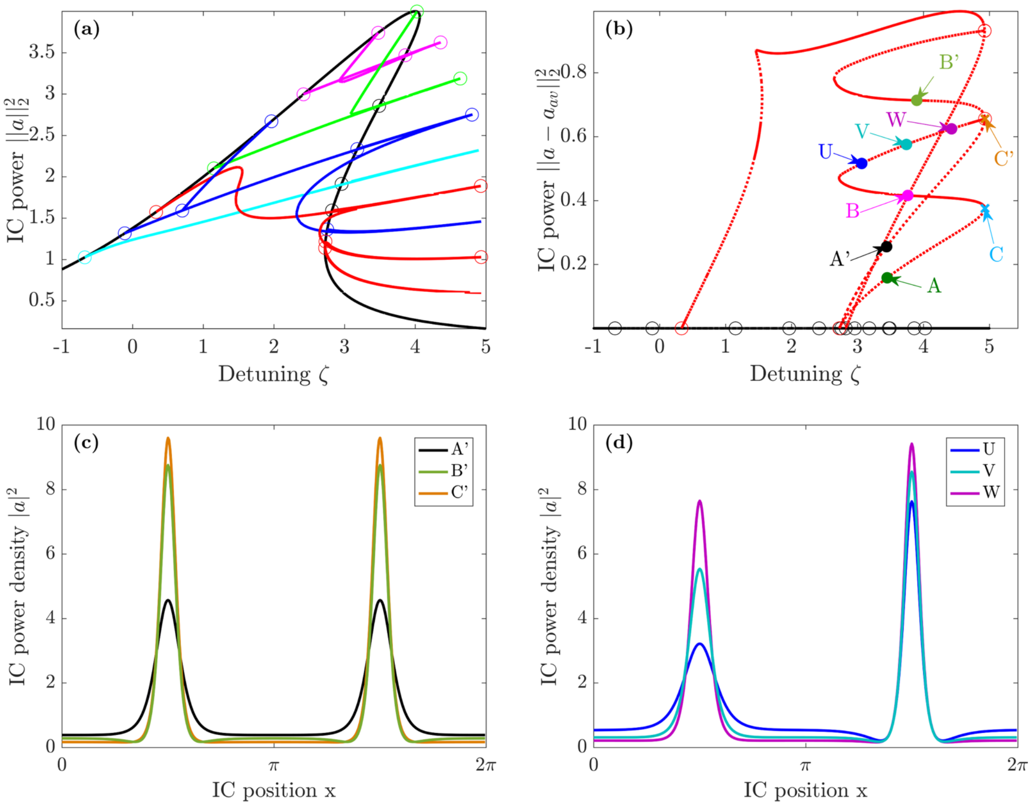

FIG. 4. Connected components of bifurcation graphs (top) and selected bright solitons (bottom) in anomalous dispersion for $f = 2$ and $d = 0.1$. Quantities on axes are dimensionless. (a) Same graph as in Fig. 1(a) shows normalized intracavity power $\|a\|_2^2$ vs normalized detuning ζ. Bifurcation points are marked as unfilled circles. Primary bifurcation points lie on the black curve of constant solutions, secondary bifurcation points lie off the black curve. Branches connected through secondary bifurcation points are plotted with the same color. (b) Detailed resolution of red connected component from (a) using the norm $\|a - a_{av}\|_2^2$ vs ζ. The black curve of constant solutions is now on the ζ axis. Stable states lie on solid lines, unstable states on dashed lines. The curve of 1-solitons runs through the states A, C, B whose spatial power distribution was shown in Fig. 1(b). Following this branch further leads to states U, V, W marking the transition from 1-solitons to 2-solitons before meeting the branch of 2-solitons through A', C', B' at the secondary bifurcation point C'. Following the A', C', B' curve further up leads to another secondary bifurcation with the branch of 4-solitons that eventually meets the trivial curve again near $\zeta_0 = 0.3325$. (c) shows the spatial power distribution of selected 2-solitons and (d) shows how on the branch of 1-solitons the transition towards 2-solitons occurs before the two branches join at point C'.

squeezing the black curve of trivial solutions onto the ζ-axis. On the other hand, it visualizes more clearly that the states before and after the turning points are different. One may even observe the snaking behavior of the branches with respect to the detuning in the range $\zeta > 2$, which is quite similar to the "foliated snaking" with respect to the forcing parameter discussed in Ref. [15, Section V.B]. Notice that in both cases secondary bifurcations occur at turning points of the curves, i.e., at local extrema of the bifurcation parameter along the curve. For the case of normal dispersion, the same comparison between $\|a\|_2^2$ and $\|a - a_{av}\|_2^2$ has been done in Figs. 5(a) and 5(b). Again, a snaking behavior can be seen on the branch of 1-solitons as well as on the 2-soliton branch, and a similar behavior (collapsed defect-mediated snaking) is described in Ref. [20] in case of bifurcation with respect to the forcing.

3. Stability

In Figs. 4(b) and Fig. 5(b), stable states are depicted with solid lines and unstable states are shown with dashed lines. Here, stability of a stationary state a means nonlinear stability, i.e., solutions of the evolution equation (1) starting in a small neighbourhood of a stay inside this neighbourhood for all times. A necessary (but not sufficient) condition for nonlinear stability of a is the spectral stability, by which we mean that the spectrum of $-\mathrm{i}L$ lies in the left complex plane, where L is the linearized operator defined in Eqs. (4) with a_0 replaced by a. Indeed, one of the main results of Ref. [25] is that for the special case of the LLE (1) spectral stability and nonlinear stability are equivalent. Notice that the shift-invariance of solutions a of Eq. (2) generates the eigenvalue 0 of the linearized operator L at any nontrivial solution. This is the reason why in Ref. [25] only orbital stability of stationary states can be deduced. In our case, we have imposed Neumann boundary conditions at $x = 0$ and $x = \pi$ together with the even symmetry around $x = \pi$. This eliminates the shift invariance so that 0 is an eigenvalue of L only at bifurcation points, and hence (with the exception of bifurcation points) proper nonlinear stability statements can be deduced. For the purpose of indicating nonlinear stability or instability in our graphs, we computed the finite spectrum of the finite-element discretization of the operator L and checked whether it belongs entirely to the lower complex plane or not.

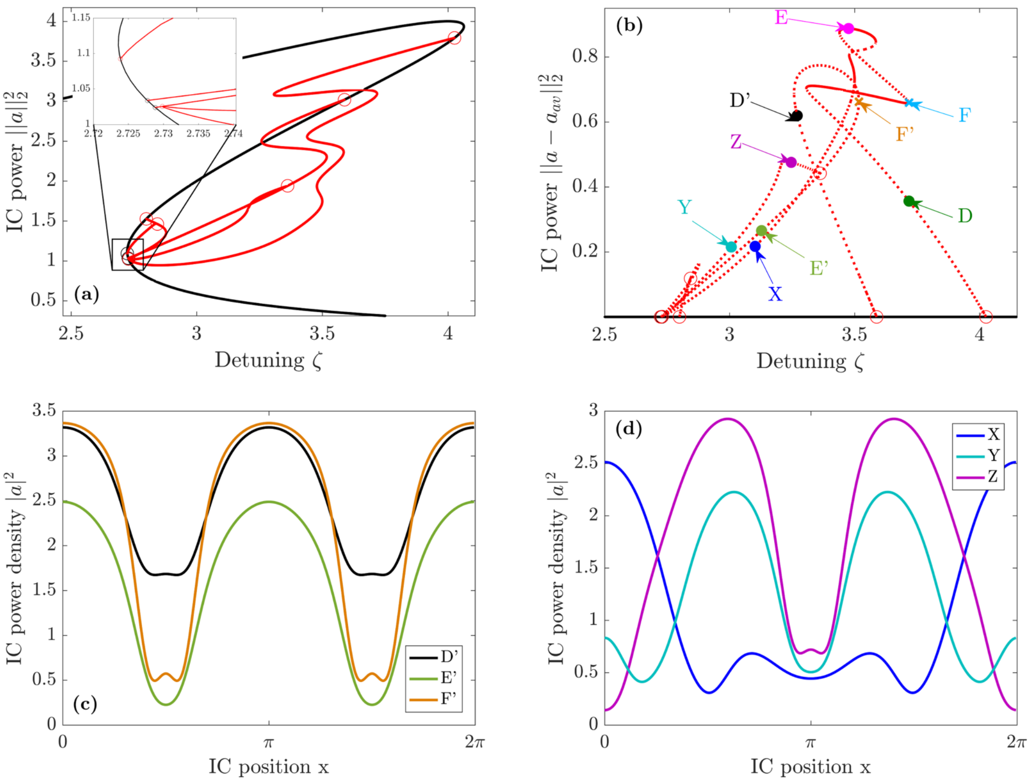

FIG. 5. Connected components of bifurcation graphs (top) and selected dark solitons (bottom) in normal dispersion for $f = 2$ and $d = -0.1$. Quantities on axes are dimensionless. (a) Same graph as in Fig. 1(d) showing normalized intracavity power $\|a\|_2^2$ vs normalized detuning ζ restricted to the relevant range. Bifurcation points are marked as unfilled circles. There are six primary bifurcation points lying on the black curve of constant solutions, and three secondary bifurcation points lying off the black curve. All branches are connected to each other and are therefore shown in red. The zoom shows how the branch of 1-solitons starting on the trivial curve near $\zeta = 4$ almost meets the curve of constant solutions near $\zeta = 2.73$. Instead, it connects at a secondary bifurcation point near $\zeta = 2.73$ with the curve of 3-solitons and immediately detaches from it again and then finally connects to the 2-solitons at the secondary bifurcation point near $\zeta = 3.36$. (b) Detailed resolution of red connected component from (a) using the norm $\|a - a_{av}\|_2^2$ vs ζ. The black curve of constant solutions is now on the ζ axis. Stable states lie on solid lines, unstable states on dashed lines. The curve of 1-solitons runs through the states D, F, E whose spatial power distribution was shown in Fig. 1(e). Following this branch further leads to states X, Y, Z marking the transition from 1-solitons to 2-solitons before meeting the branch of 2-solitons through D', F', E' at a secondary bifurcation point near $\zeta = 3.36$. (c) shows the spatial power distribution of selected 2-solitons and (d) shows how on the branch of 1-solitons the transition toward 2-solitons occurs before the two branches meet near $\zeta = 3.36$.

---

[1] J. Pfeifle, A. Coillet, R. Henriet, K. Saleh, P. Schindler, C. Weimann, W. Freude, I. V. Balakireva, L. Larger, C. Koos, and Y. K. Chembo, Phys. Rev. Lett. **114**, 093902 (2015).

[2] J. Pfeifle, V. Brasch, M. Lauermann, Y. Yu, D. Wegner, T. Herr, K. Hartinger, P. Schindler, J. Li, D. Hillerkuss, R. Schmogrow, C. Weimann, R. Holzwarth, W. Freude, J. Leuthold, T. J. Kippenberg, and C. Koos, Nat. Photon. **8**, 375 (2014).

[3] P. Marin-Palomo, J. N. Kemal, M. Karpov, A. Kordts, J. Pfeifle, M. H. Pfeiffer, P. Trocha, S. Wolf, V. Brasch, M. H. Anderson, R. Rosenberger, K. Vijayan, W. Freude, T. J. Kippenberg, and C. Koos, Nature **546**, 274 (2017).

[4] M.-G. Suh and K. J. Vahala, Science **359**, 884 (2018).

[5] P. Trocha, M. Karpov, D. Ganin, M. H. Pfeiffer, A. Kordts, S. Wolf, J. Krockenberger, P. Marin-Palomo, C. Weimann, S. Randel, W. Freude, T. J. Kippenberg, and C. Koos, Science **359**, 887 (2018).

[6] M.-G. Suh, Q.-F. Yang, K. Y. Yang, X. Yi, and K. J. Vahala, Science **354**, 600 (2016).

[7] D. T. Spencer, T. Drake, T. C. Briles, J. Stone, L. C. Sinclair, C. Fredrick, Q. Li, D. Westly, B. R. Ilic, A. Bluestone, N. Volet, T. Komljenovic, L. Chang, S. H. Lee, D. Y. Oh, M. G. Suh, K. Y. Yang, M. H. Pfeiffer, T. J. Kippenberg, E. Norberg, L. Theogarajan, K. Vahala, N. R. Newbury, K. Srinivasan, J. E. Bowers, S. A. Diddams, and S. B. Papp, Nature **557**, 81 (2018).

[8] M. H. P. Pfeiffer, C. Herkommer, J. Liu, H. Guo, M. Karpov, E. Lucas, M. Zervas, and T. J. Kippenberg, Optica **4**, 684 (2017).

[9] C. Joshi, J. K. Jang, K. Luke, X. Ji, S. A. Miller, A. Klenner, Y. Okawachi, M. Lipson, and A. L. Gaeta, Opt. Lett. **41**, 2565 (2016).

[10] J. Liu, A. S. Raja, M. Karpov, B. Ghadiani, M. H. P. Pfeiffer, B. Du, N. J. Engelsen, H. Guo, M. Zervas, and T. J. Kippenberg, Optica **5**, 1347 (2018).

[11] T. J. Kippenberg, R. Holzwarth, and S. A. Diddams, Science **332**, 555 (2011).

[12] T. Herr, V. Brasch, J. D. Jost, C. Y. Wang, N. M. Kondratiev, M. L. Gorodetsky, and T. J. Kippenberg, Nat. Photon. **8**, 145 (2014).

[13] L. A. Lugiato and R. Lefever, Phys. Rev. Lett. **58**, 2209 (1987).

[14] C. Godey, I. V. Balakireva, A. Coillet, and Y. K. Chembo, Phys. Rev. A **89**, 063814 (2014).

[15] P. Parra-Rivas, D. Gomila, L. Gelens, and E. Knobloch, Phys. Rev. E **97**, 042204 (2018).

[16] H. Guo, M. Karpov, E. Lucas, A. Kordts, V. Pfeiffer, Martin H. P. Brasch, G. Lichachev, V. E. Lobanov, M. L. Gorodetsky, and T. J. Kippenberg, Nat. Phys. **13**, 94 (2016).

[17] X. Yi, Q.-F. Yang, K. Y. Yang, M.-G. Suh, and K. Vahala, Optica **2**, 1078 (2015).

[18] C. Godey, Eur. Phys. J. D **71**, 131 (2017).

[19] P. Parra-Rivas, D. Gomila, M. A. Matias, S. Coen, and L. Gelens, Phys. Rev. A **89**, 043813 (2014).

[20] P. Parra-Rivas, E. Knobloch, D. Gomila, and L. Gelens, Phys. Rev. A **93**, 063839 (2016).

[21] R. Mandel and W. Reichel, SIAM J. Appl. Math. **77**, 315 (2017).

[22] T. Miyaji, I. Ohnishi, and Y. Tsutsumi, Physica D **239**, 2066 (2010).

[23] L. Delcey and M. Haragus, Philos. Trans. of the Roy. Soc. A **376**, 20170188 (2018).

[24] N. Périnet, N. Verschueren, and S. Coulibaly, Eur. Phys. J. D **71**, 243 (2017).

[25] M. Stanislavova and A. G. Stefanov, J. Math. Phys. **59**, 101502 (2018).

[26] X. Xue, Y. Xuan, Y. Liu, P.-H. Wang, S. Chen, J. Wang, D. E. Leaird, M. Qi, and A. M. Weiner, Nat. Photon. **9**, 594 (2015).

[27] H. Kielhöfer, *Bifurcation Theory*, Applied Mathematical Sciences, Vol. 156 (Springer, New York, 2012).

[28] P. H. Rabinowitz, J. Funct. Anal. **7**, 487 (1971).

[29] R. Mandel, Topol. Methods Nonlinear Anal. **53**, 779 (2019).

[30] H. Uecker, D. Wetzel, and J. D. Rademacher, NMTMA **7**, 58 (2014).

[31] T. Dohnal, J. Rademacher, H. Uecker, and D. Wetzel, in *Proceedings of 8th European Nonlinear Dynamics Conference (ENOC)*, edited by H. Ecker, A. Steindl, and S. Jakubek (Institute of Mechanics and Mechatronics, Vienna University of Technology, Vienna, Austria, 2014), p. 373.

[32] S. Coen and M. Erkintalo, Opt. Lett. **38**, 1790 (2013).

[33] C. Bao, L. Zhang, A. Matsko, Y. Yan, Z. Zhao, G. Xie, A. M. Agrawal, L. C. Kimerling, J. Michel, L. Maleki, and A. E. Willner, Opt. Lett. **39**, 6126 (2014).

[34] K. Nozaki and N. Bekki, J. Phys. Soc. Jpn **54**, 2363 (1985).

[35] K. Nozaki and N. Bekki, Physica D **21**, 381 (1986).

[36] X. Xue, P.-H. Wang, Y. Xuan, M. Qi, and A. M. Weiner, Laser Photonics Rev. **11**, 1600276 (2017).

[37] J. Gärtner, R. Mandel, and W. Reichel, The Lugiato-Lefever equation with nonlinear damping caused by two photon absorption, arXiv:1811.12200.

[38] M. G. Crandall and P. H. Rabinowitz, J. Funct. Anal. **8**, 321 (1971).

[39] H. Brezis, *Functional Analysis, Sobolev Spaces and Partial Differential Equations*, Universitext (Springer, New York, 2011).

[40] T. Hansson and S. Wabnitz, Nanophotonics **5**, 231 (2016).